Volume 5
Number 9
September 2020
Pages 1517–1860

Reaction Chemistry & Engineering

Linking fundamental chemistry and engineering to create scalable, efficient processes

rsc.li/reaction-engineering

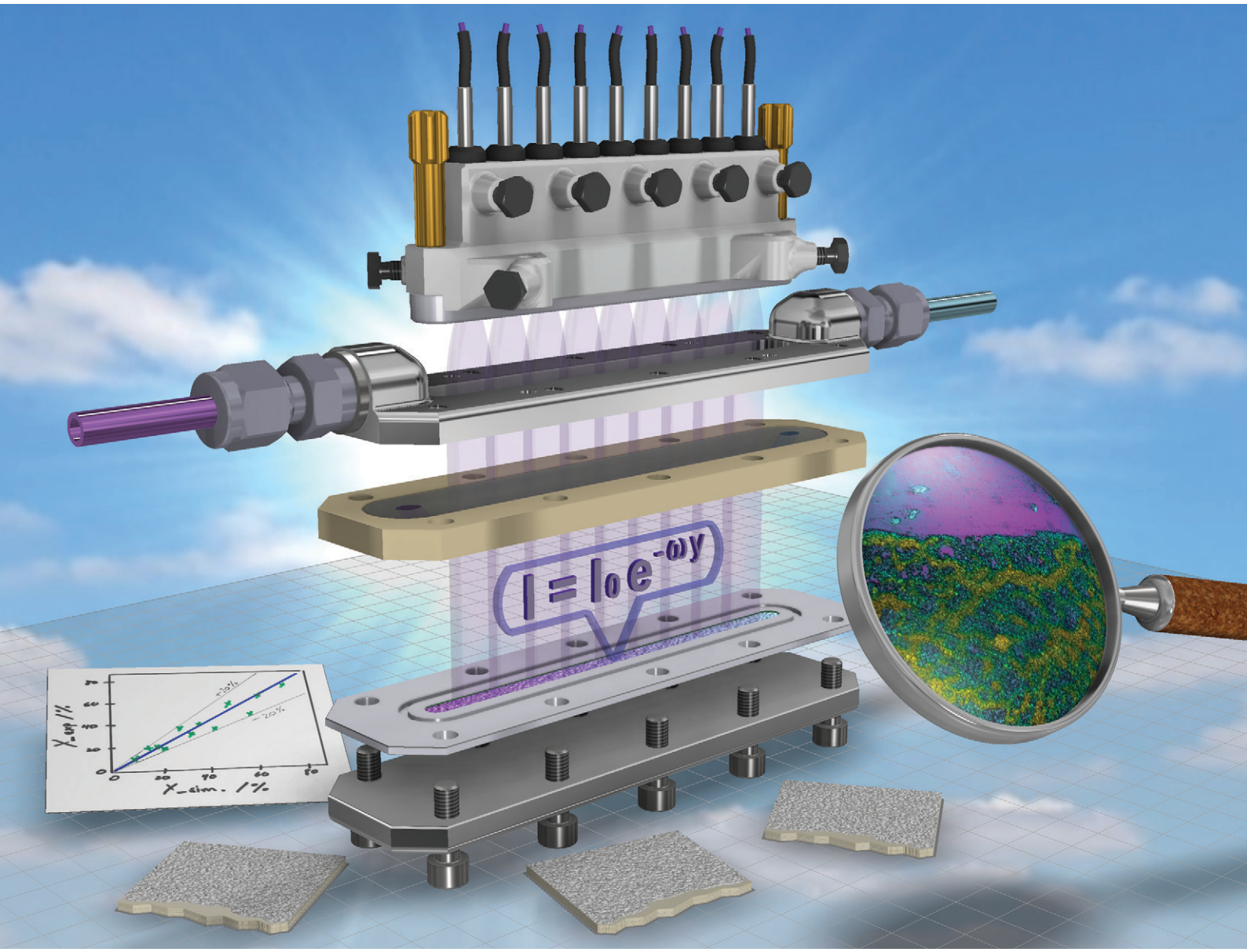

ISSN 2058-9883

ROYAL SOCIETY OF CHEMISTRY

PAPER

Michael Klumpp *et al.*

Investigation of the reaction kinetics of photocatalytic pollutant degradation under defined conditions with inkjet-printed TiO_2 films – from batch to a novel continuous-flow microreactor

Reaction Chemistry & Engineering

ROYAL SOCIETY OF CHEMISTRY

PAPER

View Article Online
View Journal | View Issue

Open Access Article. Published on 11 August 2020. Downloaded on 4/29/2026 1:24:24 PM.
This article is licensed under a Creative Commons Attribution-NonCommercial 3.0 Unported Licence.

Check for updates

Cite this: *React. Chem. Eng.*, 2020, 5, 1658

Investigation of the reaction kinetics of photocatalytic pollutant degradation under defined conditions with inkjet-printed TiO_2 films – from batch to a novel continuous-flow microreactor†

Xiang Zhan, [a] Chenhui Yan,[a] Yilin Zhang,[a] Günter Rinke,[a] Georg Rabsch,[a] Michael Klumpp, *[ab] Andrea Iris Schäfer[c] and Roland Dittmeyer [ab]

Received 5th June 2020,
Accepted 29th July 2020

DOI: 10.1039/d0re00238k

rsc.li/reaction-engineering

Pollutants accumulating in natural and drinking water systems can cause severe effects to the environment and living organisms. Photocatalysis is a promising option to degrade such pollutants. When immobilizing the photocatalyst, additional catalyst separation steps can be avoided. Among various reactor types, the use of microreactors in photocatalysis has proven advantageous regarding process intensification. However, so far the local conditions are not well understood and described in literature and there is little quantitative understanding of the relevant phenomena. In this work, inkjet-printing was used to immobilize TiO_2 as a thin film with a precisely tuneable thickness and catalyst loading. In a batch reactor, the degradation of rhodamine B (RhB) as a model pollutant was performed for different initial concentrations and catalyst layer thicknesses. By employing the Langmuir–Hinshelwood model and a light irradiation model, the kinetic parameters were determined. The influence of the light intensity at different positions inside the immobilized photocatalyst on the reaction kinetics is quantified. RhB degradation was tested under defined operational conditions using an in-house developed continuous-flow microreactor with advanced fiber optics for precise light introduction. The models derived from batch experiments were used to simulate the degradation in the continuous-flow microreactor. Results show that the simulation allows prediction of the performance with less than 20% deviation to the experimental data. An analysis of mass transport effects on the reaction rate indicates that external mass transfer is a limiting factor in the microreactor experiment. This study further demonstrates the potential of the new reactor system (microreactor, fiber optics and printed catalyst) for detailed investigations on photocatalytic reaction kinetics.

1. Introduction

Water pollution is one of the critical reasons for the global burden of diseases.[1] In both developing and industrialized countries, an increasing number of contaminants are emerging in the water bodies: from traditional compounds such as dyes and heavy metals, to pollutants of low concentration such as pharmaceuticals.[2] They can accumulate in the environment with short- and long-term effects both on human beings and on wildlife.[2,3]

Traditional decontamination methods based on physical separation and biological oxidation are not efficient in completely "destroying" such pollutants, especially non-biodegradable micropollutants.[4,5] Chemical purification technologies such as chlorination and ozonation suffer from high operational cost and could generate toxic secondary pollutants ending up in the ecosystem.[6] Membrane filtration such as nanofiltration and reverse osmosis can achieve high removal of micropollutants at high energy requirements,[7–9] while adsorption incorporated into membrane materials can significantly lower the energy requirements.[10,11] In comparison, photocatalysis being one of the "Advanced Oxidation Processes (AOPs)" is considered as an innovative decontamination technology able to degrade pollutants to some extent. In particular, heterogeneous photocatalysis

[a] *Institute for Micro Process Engineering (IMVT), Karlsruhe Institute of Technology (KIT), Eggenstein-Leopoldshafen, 76344, Germany.*
E-mail: michael.klumpp@kit.edu
[b] *Institute of Catalysis Research and Technology (IKFT), Karlsruhe Institute of Technology (KIT), Eggenstein-Leopoldshafen, 76344, Germany*
[c] *Institute for Advanced Membrane Technology (IAMT), Karlsruhe Institute of Technology (KIT), Eggenstein-Leopoldshafen, 76344, Germany*
† Electronic supplementary information (ESI) available. See DOI: 10.1039/d0re00238k

This journal is © The Royal Society of Chemistry 2020

Open Access Article. Published on 11 August 2020. Downloaded on 4/29/2026 1:24:24 PM.
This article is licensed under a Creative Commons Attribution-NonCommercial 3.0 Unported Licence.

based on semiconducting materials has proven high efficiency in water treatment.[6,12] Of all the photocatalysts, TiO_2 has been most extensively studied because of its low cost and low toxicity, high activity and chemical stability.[13]

In TiO_2-based photocatalytic reactors, TiO_2 nanoparticles dispersed in the liquid phase (*i.e.*, slurry reactors) is one common approach. However, in this case, the catalyst needs to be removed from the water after the reaction for reuse by *e.g.*, filtering.[14] This additional step adds complexity and cost to the overall process. Immobilizing the catalyst as a coating can avoid extra catalyst separation. TiO_2 has been coated on various substrates including glass slides,[15,16] nanofibers,[17] polymer[18] and ceramic membranes,[19–23] and used for water decontamination either in batch,[16,18,22] or continuous-flow reactors.[15,17–21,23,24] However, there are three obvious constraints of continuous-flow reactors with immobilized photocatalysts:[25]

1) external mass transport may limit the overall reaction kinetics especially in laminar flow conditions at low fluid flow rate, since the diffusion of the reactant from the bulk fluid to the catalyst layer may not be sufficiently fast;

2) internal mass transport resistance inside the catalyst layer depends on layer thickness and may be significant as well;

3) photon transmission likewise depends on the layer thickness and may decrease dramatically due to *e.g.*, diffraction in the porous layer, which may compromise the light utilization efficiency.

Microreactors, more precisely microstructured reactors, allow for efficient mass transport even in laminar flow conditions. In general, microreactors have one or multiple channels of only several ten up to a few hundred of micrometers in width or/and depth.[26] Due to the reduced diffusion path length from the bulk pollutant solution to the catalyst layer, mass transport limitations can be largely reduced, which overcomes one major drawback of catalyst immobilization.[27] Continuous-flow microreactors with immobilized TiO_2 layers have been applied for photocatalytic water treatment previously.[19,24,28–30] According to a recently published comparative study on different reactors for photocatalytic water treatment with TiO_2,[31] a microreactor has shown superior performance in reaction kinetics when compared to conventional batch and continuous stirred-tank reactors (CSTR). Yet to match the requirements of practical applications regarding throughput a proper strategy for scaling-up and/or numbering-up of microchannel-based systems is needed.[4,31]

Kinetic studies are essential to understand the local conditions and processes for photocatalytic pollutant degradation in different reactor systems. Relevant works have been conducted in the past 20 years, which have been recently reviewed by Visan *et al.*[32] However, regardless of the reactor system considered, most published works used a pseudo-first-order reaction model simplified from the Langmuir–Hinshelwood model, which may not always be adequate as the adsorption constant can have a significant contribution to the kinetics.[33] For systems with immobilized photocatalyst, kinetic studies can be more complicated than slurry systems because of two reasons, namely, the decay of light intensity inside the catalyst layer and the presence of internal mass transport limitations. These two aspects also correlate with the thickness of the coating and are often not in the focus of the works published so far. Ray *et al.*[25,34–36] and Visan *et al.*[24] have studied explicitly the reaction kinetics and developed reactor models for photocatalytic pollutant removal by including the influence of layer thickness, mass transport and decay of light intensity. In general, there is a lack of validation of the models proposed using other reactor systems in order to demonstrate their universal applicability. For a more detailed discussion of how to report and compare photocatalytic performances between different reactor systems considering defined experimental conditions including the catalyst, model pollutant, light type, and intensity the reader is referred to ref. 37 and 38.

A prerequisite for a detailed kinetic study on the influence of the layer thickness is a precise control of the coating thickness. Conventional coating techniques such as dip coating,[20] chemical vapor deposition,[21] magnetron sputtering[22] and spin coating[24] either cannot satisfy this purpose or suffer from other disadvantages such as limitation in substrate geometry, complex preparation of precursors, or inhomogeneity of the coatings. Being a rather new coating method, inkjet-printing is considered as a cost-effective and convenient technology.[39,40] The "drop-on-demand" printing of nanoparticles allows to form a homogeneous layer with precisely controllable catalyst loading and layer thickness, which is a prerequisite for kinetic studies.[25,41]

Kinetic studies can also be found for microreactors with immobilized photocatalyst.[24,42,43] For microreactors, although external mass transport limitations are often considered (see, *e.g.*, ref. 44), internal (pore) diffusion limitations are not always discussed. Additionally, for microreactors which are generally fabricated in the form of microfluidic chips, while varying the inlet concentration and flow rate is convenient, one constraint with them is a possible non-uniformity of the illumination since part of the light irradiates the non-active area of the reactor when the light source (most commonly a lamp) is placed above the chip. This configuration can decrease the light utilizing efficiency and poses a challenge to kinetic study and reactor modeling. Approaches to optimize the illumination include, *e.g.*, the use of micro-LED arrays[31,45] or optical fibers with proper lenses to focus the light homogeneously on the reactive area.

The present work studies the reaction kinetics of photocatalytic pollutant degradation. TiO_2 was used as the model photocatalyst in the form of immobilized thin films prepared by inkjet-printing. The degradation of a model dye pollutant rhodamine B (RhB) was performed with these films in a batch reactor by varying the initial pollutant concentration and the thickness of the coating. Kinetic

Open Access Article. Published on 11 August 2020. Downloaded on 4/29/2026 1:24:24 PM.
This article is licensed under a Creative Commons Attribution-NonCommercial 3.0 Unported Licence.

parameters were determined by fitting the parameters of a Langmuir–Hinshelwood model to the experimental data. Next, RhB degradation was performed in a novel continuous-flow microreactor system, which can operate under well-defined conditions with precisely controlled light intensity *via* fiber optics. The kinetic model derived from the batch experiments was validated with the results from the microreactor by varying operational parameters. The influence of the internal and external mass transport limitations on the observed kinetics was discussed for both reactors.

2. Experimental

2.1. Immobilization of TiO_2 by inkjet-printing

Commercial TiO_2 P25 (Evonik) was used as the photocatalyst. Following procedures from literature,[16,46] the ink suspension was prepared by adding the TiO_2 powder, a dispersant (Zetasperse 1200, Air Products), an electrolyte $Na_4P_2O_7$ (Sigma-Aldrich), two co-solvents *N*,*N*-dimethylformamide (VWR Chemicals) and PEG-400 (Sigma-Aldrich) to deionized water (Milli-Q, Merck). Traces of NaOH solution (1 M) were used to adjust the pH value. All chemicals were used as received without further purification (electrolyte, co-solvents and NaOH: analytical grade). The as-prepared ink was ultrasonicated (Elmasonic P) at 80 kHz for 20 min before it was used for printing.

The TiO_2 ink composition was investigated first to determine the optimum concentration of the individual components. The explored ranges and the optimum values are summarized in Table 1. The optimized composition was determined by measuring the particle size and zeta potential at various pH values using a Delsa Nano instrument (Beckman Coulter) (see also ESI† S1), and testing the ink printability by monitoring the stability of droplet generation with the CCD camera. Thermogravimetric analysis (TGA, Setsys Evolution 16/18, Setaram) was conducted for the developed ink in order to investigate the removal of the inks' additives upon calcination. The viscosity of the optimized ink was 1.60 mPa s measured at a shear rate of 100 s^{-1} (HAAKE RheoStress 1, Thermo Scientific), which lies in the manufacturer-recommended range (0.4–100 mPa s) for the nozzle. The density of this ink was 1.07 g mL^{-1}.

An Autodrop Compact (Microdrop Technologies) drop-on-demand inkjet-printer was used for printing. A detailed description of the printing process can be found in the ESI† S2. Briefly, ink droplets were generated by impulses induced by the piezoelectric dispenser head. The specific voltage and pulse length of one impulse was tuned in order to achieve stable droplet formation (see ESI† Fig. S3), which was monitored by a high-speed CCD camera attached to the printing system.

For the present study, a suitable substrate is expected to fulfill four requirements: 1) sufficient thermal stability since the coating has to be calcined after printing; 2) permeability to water as to enable operation in cross-flow filtration mode in a later stage of the project; 3) well-defined porous structure which allows for good adhesion of the layer and facilitates the generation of a homogeneous layer by absorbing the suspension agents; 4) suitable pore size which avoids the TiO_2 particles to penetrate into the pores. Accordingly, for this work, commercial ceramic nanofiltration membrane sheets (Fraunhofer IKTS) with an average pore size of 0.9 nm were used as substrate. They consist of a 1 mm thick macro- and mesoporous alumina support covered by a titania nanofiltration layer of approx. 20–50 nm thickness. The same substrate was also used elsewhere for coating TiO_2 by magnetron sputtering.[22] Substrates were laser-cut into sizes of 2.5 cm × 2.5 cm and 10.8 cm × 0.8 cm, respectively (see ESI† Fig. S3), and cleaned by rinsing the surface with acetone and deionized water before printing. Layer-by-layer printing was conducted to achieve the desired layer thickness. In order to increase the adhesion of the TiO_2 layer to the substrate and to remove the additives in the inks, the printed samples were calcined in a muffle oven (Heraeus) with a heating rate of 2 K min^{-1} to 250 °C being held for 30 min. This temperature was determined by following the degradation of RhB in the batch reactor with samples calcined at various temperatures (see ESI† S4 for details).

2.2. Characterization of the coatings

Scanning electron microscope (SEM) images of the printed layers were taken by a JSM 6300 instrument (Jeol) applying a 10 kV beam. Electron probe microanalysis (JXA 8530F, Jeol) with 15 kV was used for cross-sectional elemental analysis. 2D as well as 3D surface maps of the printed layer were obtained with an S-neox 3D optical profilometer (Sensofar) in confocal mode. From the topological data obtained, the layer thickness was determined (see ESI† S7 for details). X-ray diffraction (XRD) patterns of the catalyst powder were gathered using a Bruker D8 Advance X-ray diffractometer

Table 1 Composition of the TiO_2 ink

Material	Function	Investigated range (wt%)	Optimized value
TiO_2 P25	Catalyst	0.1–1.0	0.5 wt%
Water	Main solvent	—	88.5 wt%
Zetasperse 1200	Surfactant	0.5–4.0	2 wt%
$Na_4P_2O_7$	Electrolyte to enhance the electrostatic stability	—	5×10^{-4} M
PEG 400	Co-solvent to enhance the steric stability	5–10	7 wt%
DMF	Controls drying and modifies surface tension	0.5–5.0	2 wt%
NaOH	Adjusting pH	—	10 (±0.3)

 This journal is © The Royal Society of Chemistry 2020

Open Access Article. Published on 11 August 2020. Downloaded on 4/29/2026 1:24:24 PM.
This article is licensed under a Creative Commons Attribution-NonCommercial 3.0 Unported Licence.

with Cu Kα radiation operated at 40 kV and 40 mA. The data were recorded in the 2θ range of 20–80° with a scanning rate of 4° min^{-1}. X-ray photoelectron spectroscopy (XPS) (Scienta 4000, Al Kα line) analysis was carried out to determine whether elements other than Ti and O are present in the coating, *e.g.*, due to the additives present in the ink. A UV-vis spectrophotometer (HP, 8453) was used for measuring the UV light transmission T_L [%] of the coating with 1–9 layers on quartz glass, which was immersed into the model pollutant solution in a quartz cuvette during the measurement (see also ESI† S8). The transmission was measured at 365 nm wavelength and normalized based on the blank test using an identical quartz glass without coating.

2.3. Degradation in batch reactor

First, the photocatalytic reaction kinetics was evaluated by following the degradation of RhB (Merck) aqueous solution in a batch reactor. A halogen lamp (VL-115.L, Vilber Lourmat) emitting UV light of 365 nm wavelength was used as the light source. As shown in Fig. 1, the as-prepared sample (printed TiO_2 on the substrate) was immersed 3 mm beneath the pollutant solution (total volume: 14 mL) and held by a sample holder made of stainless steel. The light intensity was 3.5 mW cm^{-2} at the very position of the sample, as measured by a UV irradiation meter TM213 (Tenmars). The solution temperature was kept at 23 °C by recirculating water *via* a Polystat CC1 (Huber).

Prior to irradiation, the solution was magnetically stirred in the dark for 60 min, which – according to preliminary tests – is sufficient for the establishment of an adsorption/desorption equilibrium between the immersed sample and the pollutant. 1 mL RhB solution was taken at certain intervals for concentration measurement and given back to the beaker afterwards in order to maintain a constant liquid level. A stirring speed of 200 rpm was used throughout the work. Variation of the calcination temperature (150–300 °C), initial RhB solution concentration (3, 6, 12, 15 g m^{-3}) and thickness of the TiO_2 layers (110–990 nm) on the degradation were performed. Blank tests were conducted by irradiating the substrate without any catalyst coating. The degradation in blank test was not significant (see ESI† Fig. S4), and hence will not be presented in the following graphs.

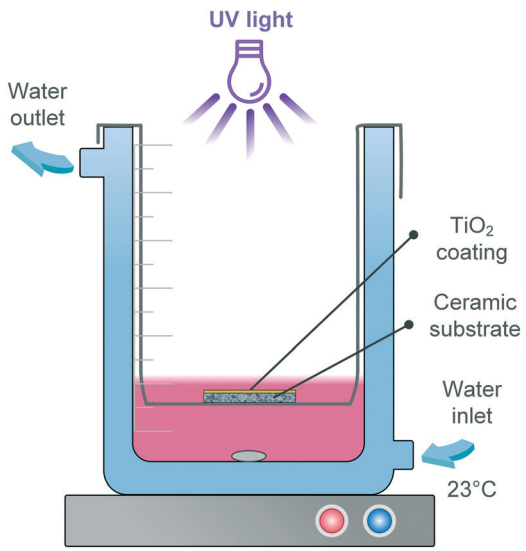

Fig. 1 Illustration of the batch reactor set-up.

2.4. Degradation in the continuous-flow microreactor

In this work, a continuous-flow microreactor shown in Fig. 2 and in the ESI† S9–S12 was developed. Light was introduced into the reactor *via* 9 optical fibers (numerical aperture = 0.63, core diameter 1 mm, Prizmatix) and focused by cylindrical lenses made of quartz glass (H-K9L, Worldhawk). The fibers were held by a 3D-printed polymeric holder (material: Veroclear, Stratasys) and fixed by PVC screws. Every 3 fibers were split from one main fiber connected directly to the light source. In order to make the light illumination area exactly match the microchannel area, and thereby enhancing the photonic energy utilization efficiency, the lenses were selected considering the focal length and light output angle from the fibers. The microchannel was fabricated inside a PTFE substrate holder covered by a quartz plate with two cylindrical oblique holes for the inlet and outlet flow. The substrate coated by 9 TiO_2 layers was put into the holder and sealed by epoxy sealing (UHU45700). O-Rings were used to seal the quartz plate with the PTFE holder and the metallic part for inlet and outlet flow, respectively.

It has to be noted that this reactor was designed and fabricated with a second microchannel beneath the coated substrate, which can be used for cross-flow filtration operation as mentioned above. As this feature was not needed for the present work, only the upper channel was used, and hence the illustration of the reactor structure (Fig. 2a–c) is simplified without showing the second channel.

A continuous-flow system for pollutant degradation was established (ESI† Fig. S11). The light source used was a high-power LED emitting 365 nm UV light (Prizmatix). The light intensity can be tuned with an accuracy of 1%. The pollutant solution was fed into the reactor with variable flow rates by a K-120 HPLC pump (Knauer). Prior to illumination, the solution was kept flowing at 0.5 mL min^{-1} for *ca.* 60 min (based on preliminarily tests) to ensure that the adsorption/desorption equilibrium throughout the system was reached. The sample was taken from the outlet continuously until the concentration was stable (±5% for 3 consecutive samples). The experiments in the microreactor were conducted under defined conditions by varying the light intensity (0.5 and 1.5 mW cm^{-2}), flow rate (0.05, 0.1 and 0.2 mL min^{-1}) and inlet concentration of RhB (3 and 15 g m^{-3}).

3. Modelling

3.1. Light irradiation model

In photocatalysis, the reaction rate does not only depend on the concentration of the reactants and temperature, but also

Open Access Article. Published on 11 August 2020. Downloaded on 4/29/2026 1:24:24 PM.
This article is licensed under a Creative Commons Attribution-NonCommercial 3.0 Unported Licence.

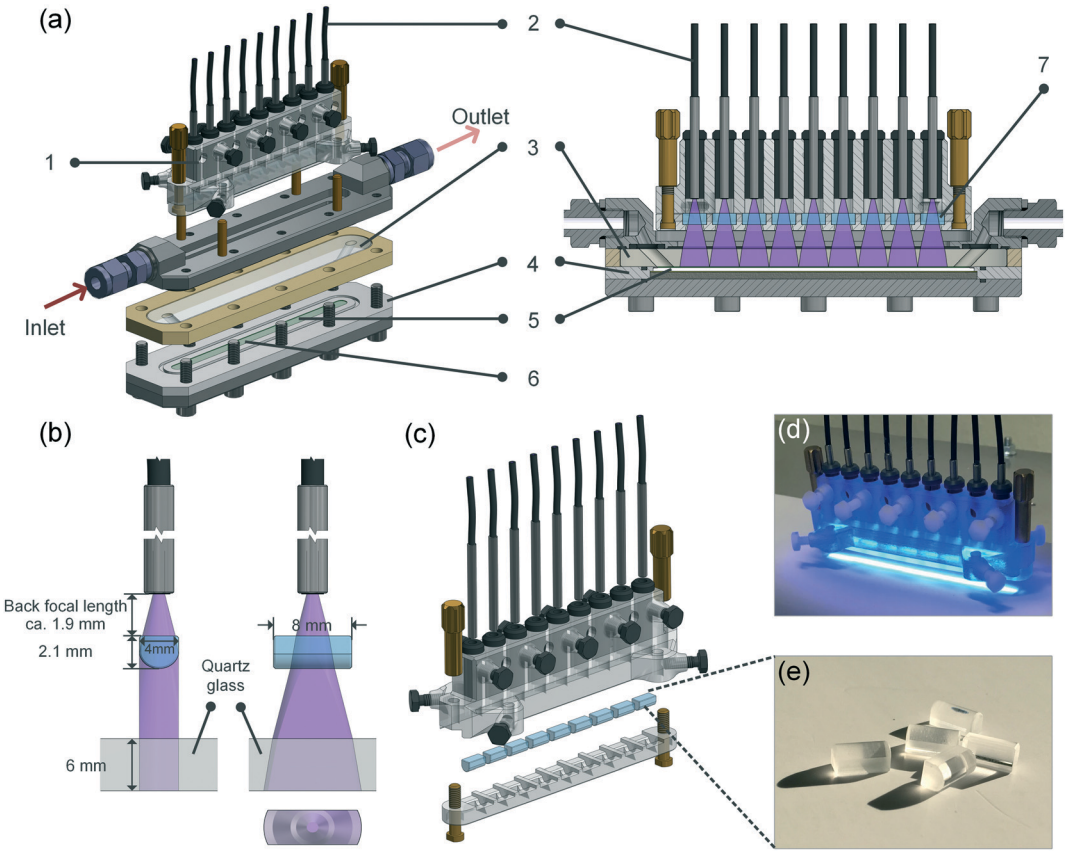

Fig. 2 Continuous-flow microreactor system used in this work: (a) simplified structure of the reactor: 1. 3D-printed polymeric fiber holder; 2. optical fiber; 3. quartz glass; 4. PTFE holder; 5. ceramic substrate with printed TiO_2; 6. microchannel (100 mm × 5 mm × 0.3 mm); 7. cylindrical lens; (b) illustration of the light path from the fiber to the channel *via* the lens; (c) illustration of the optical part; (d) picture of the optical part with light on (blue light was used in the picture for a better color contrast); (e) quartz cylindrical lenses.

on the number of photons hitting the catalyst surface per unit of time as well as on the energy of these photons. The effects of the number of photons per unit of time and of the energy of the photons on the reaction rate can be separated from the concentration and temperature influence by introducing a dependency of the reaction rate constant k [g g^{-1} s^{-1}] on the light intensity I [mW cm^{-2}] and wavelength λ [nm] as follows:[47]

$$k = aI^b \tag{1}$$

a [g cm^{2b} g^{-1} s^{-1} mW^{-b}] and b [–] are constants to be determined from experiments. b is unitless whereas the unit of a depends on the value of b. For the case of immobilized photocatalyst, the light intensity I decays along the irradiation direction y toward the bottom of the layer, which can be reflected by using the Beer–Lambert-Law (Fig. 3):

$$I = I_0 e^{-\omega y} \tag{2}$$

Here, I_0 [mW cm^{-2}] is the incident light intensity and ω [m^{-1}] is the extinction coefficient, which can be determined by fitting the measured transmission T_L to the layer thickness δ_L [m] according to the following equation:

$$-\ln(T_L) = \omega\delta_L \tag{3}$$

The effective rate constant $\bar{k}$ [g g^{-1} s^{-1}] of a catalyst layer with thickness of δ_L is then found by integrating eqn (1) over the layer thickness:

$$\bar{k} = \frac{1}{\delta_L}\int_0^{\delta_L} k(y)dy = \frac{1}{\delta_L}\int_0^{\delta_L} aI_0{}^b e^{-b\omega y} dy = \frac{aI_0{}^b}{b\omega\delta_L}\left(1 - e^{-b\omega\delta_L}\right) \tag{4}$$

The parameters a and b can be determined from experiments carried out with different layer thickness δ_L at constant temperature and wavelength λ in the absence of mass transport limitations. Such conditions prevailed in the batch

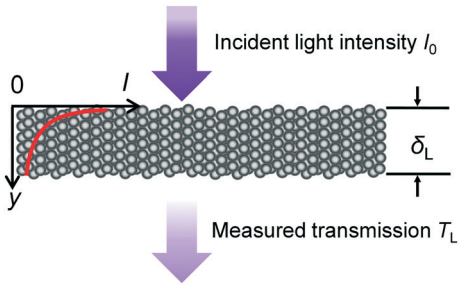

Fig. 3 Light penetration through the photocatalyst layer.

This journal is © The Royal Society of Chemistry 2020

Open Access Article. Published on 11 August 2020. Downloaded on 4/29/2026 1:24:24 PM.
This article is licensed under a Creative Commons Attribution-NonCommercial 3.0 Unported Licence.

reactor experiments performed in this study, as shown in section 3.2.

To develop the light irradiation model for this study, the following assumptions have to be made additionally:

- the UV lamp works stable and its irradiance is constant during the experiment;
- the illumination is equally distributed at the geometric surface of the catalyst layer with the incident intensity I_0;
- the structure of the catalyst layer is uniform.

3.2. Reaction kinetics

The concentration of the RhB solution from batch and microreactor experiments in this work was determined using a UV-vis spectrophotometer (HP, 8453) at 554 nm by measuring the absorbance. The concentration was calculated by the measured absorbance using the Lambert–Beer law which correlates absorbance with concentration. It has to be noted that in this work the degradation of RhB refers to the decolorization. Moreover, temperature changes during the experiments performed in this study which could affect the kinetics were found to be insignificant based on temperature measurements of the RhB solution for both reactor systems (±2 K).

The following Langmuir–Hinshelwood (LH) expression is a widely used model for describing heterogeneous photocatalytic reactions.[48,49] For a monomolecular irreversible degradation reaction, r_{int} [g s^{-1}], according to eqn (5), is the intrinsic reaction rate:

$$r_{int} = \frac{k_{int} m_{cat} K_{LH} C}{1 + K_{LH} C} \quad (5)$$

where k_{int} [g g^{-1} s^{-1}] is the intrinsic (catalyst-mass-related) rate constant, m_{cat} [g] is the catalyst mass, K_{LH} [m^3 g^{-1}] is the adsorption equilibrium constant of the reactant, and C [g m^{-3}] is the mass concentration of the pollutant in the liquid phase. Note that the reaction rate is always positive. When applying eqn (5) to the printed catalyst layers of this study, k_{int} has to be replaced with $\bar{k}$ from eqn (4).

As opposed to the intrinsic reaction rate, the observed rate of consumption of the pollutant in the batch reactor R_{obs} [g s^{-1}] is defined in accordance with the material balance for the pollutant:

$$R_{obs} = V_{batch} \frac{dC_b}{dt} \quad (6)$$

where V_{batch} [m^3] is the constant volume of the reactant solution in the batch experiment, and dC_b/dt represents the observed differential change of the bulk concentration C_b [g m^{-3}] with time t [s] in the reactor. Eqn (6) assumes that for a given time t the bulk concentration is the same everywhere in the reactor due to vigorous stirring.

If concentration gradients inside the catalyst layer as well as a concentration difference between the bulk liquid and the geometric surface of the catalyst layer can be neglected, the liquid phase concentration C in eqn (5) is identical to the bulk liquid concentration C_b in eqn (6), and the observed reaction rate is identical to the intrinsic reaction rate. This allows to combine eqn (4)–(6) to the following eqn (7):

$$\frac{dC_b}{dt} = -\frac{1}{V_{batch}} \frac{a {I_0}^b \left(1 - e^{-b\omega\delta_L}\right)}{b\omega\delta_L} \frac{m_{cat} K_{LH} C_b}{1 + K_{LH} C_b} \quad (7)$$

Estimates for the constants a, b and K_{LH} were obtained by fitting the solution of eqn (7), which was obtained from the Matlab® ODE45 solver, to the concentration profiles measured for different catalyst layer thicknesses and initial concentrations in the batch reactor. A weighted least squares approach was adopted for the objective function to be minimized, *i.e.*, $RSS = \sum_i \left[\left(C_{b.exp.i} - C_{b.sim.i}\right)/\Delta C_{b.exp.i}\right]^2$, in which $\Delta C_{b.exp.i}$ is the measured standard error of the experimentally observed concentration $C_{b.exp.i}$ at time point i (based on 3 replicate measurements), $C_{b.sim.i}$ is the corresponding concentration from the model.

Prior to this, the absence of external (film) diffusion limitations had been verified experimentally by increasing the stirring speed until there was no further increase of the reaction rate (section 4.3). Moreover, the absence of internal (pore) diffusion limitations was verified by assessing the Weisz modulus. Its generalized definition is given in eqn (8):[50]

$$\Psi_{WP} = \left(\frac{V_{cat}}{A_{cat.ext.}}\right)^2 \frac{n+1}{2} \frac{r_{obs}}{D_{eff} C_s} \quad (8)$$

V_{cat} [m^3] is the volume of the catalyst layer, $A_{cat.ext.}$ [m^2] is the external surface area of the catalyst layer, n is the reaction order, r_{obs} [g s^{-1} m^{-3}] is the observed reaction rate divided by the catalyst volume, D_{eff} [m^2 s^{-1}] is the effective diffusion coefficient of RhB in the catalyst layer, and C_s [g m^{-3}] is the mass concentration of the pollutant on the external catalyst surface. Note that a catalyst layer with thickness δ_L which is accessible for the reactant only from the top surface essentially behaves like a flat catalyst plate of thickness $2 \times \delta_L$ for reasons of symmetry. Thus, for calculation of ψ_{WP} in the present work, $V_{cat}/A_{cat.ext.}$ was replaced by $2\delta_L$.

The effect of internal diffusion on the observed reaction rate can be neglected if the Weisz modulus is equal to or smaller than a certain limiting value. The meaning of the limiting value is that the observed reaction rate will not be lower by more than 5% compared to the conditions prevailing at the external surface due to the decline of the concentration inside the catalyst caused by the finite diffusion rate. For a monomolecular irreversible reaction following LH-type kinetic expression, the limiting value depends on the product of $K_{LH}C$, which is essentially $K_{LH}C_b$ for the batch reactor experiments as previously discussed.[51] Satterfield[52] analyzed this type of reaction for a flat catalyst plate and presented a solution of effectiveness factors with regard to the Weisz modulus for different values of $K_{LH}C$, which was used to derive limiting values in this work. Generally, the smaller the value of $K_{LH}C$, the lower the limiting value. For all batch reactor experiments performed in this study, the lowest limiting values were present at the

Open Access Article. Published on 11 August 2020. Downloaded on 4/29/2026 1:24:24 PM.
This article is licensed under a Creative Commons Attribution-NonCommercial 3.0 Unported Licence.

end of each experiment, when the concentrations were the lowest. The values of the Weisz modulus for different layer thickness (from 110 to 990 nm) calculated for the end of each experiment always stayed below the limiting values, as shown later in section 4.3.

Based on this observation, we can safely conclude that the kinetic data obtained from the batch experiments are not affected by pore diffusion. This holds even more as the reaction rate in our case, even in the absence of concentration gradients, decreases further inside the catalyst layer due to the attenuation of the light which lowers the rate constant, as shown in section 3.1. This is not considered in the simple estimation based on the Weisz modulus, but leads to a slowing down of the reaction rate further inside the layer while the diffusion rate remains unchanged.

For the microreactor, the material balance for the pollutant reads:

$$\frac{dC_b}{dz} = \frac{1}{\dot{V} L_{MR}} R_{obs} \tag{9}$$

An influence of pore diffusion on the observed reaction rate R_{obs} can be safely excluded for the microreactor experiments as well, because the light intensity in the microreactor was lower than in the batch reactor (meaning lower reaction rate) while the pollutant concentration was comparable and the layer thickness was the same (*ca.* 990 nm).

However, the situation is different for external mass transport, because of the low flow velocities applied in the microreactor. This is why R_{obs} in eqn (9) cannot be related directly to the bulk liquid concentration C_b. Instead, the unknown pollutant concentration C_s on the external surface of the printed catalyst layer has to be determined. This was achieved by equating the diffusive flux to the external surface of the layer and the rate of consumption in the layer related to its external surface area. The same approach was also taken, *e.g.*, by Charles *et al.*:[44]

$$\beta_m (C_b - C_s) = \frac{\bar{k} m_{cat} K_{LH} C_s}{1 + K_{LH} C_s} \frac{1}{A_{cat}} = \frac{\delta_L \rho_{cat} \bar{k} K_{LH} C_s}{1 + K_{LH} C_s} \tag{10}$$

Here, β_m [m s^{-1}] is the mass transfer coefficient, A_{cat} [m^2] is the external surface area of the catalyst layer and ρ_{cat} [g m^{-3}] is the density of the catalyst layer which is calculated in section 4.2. After rearranging, a quadratic equation for calculating C_s is obtained:

$$C_s{}^2 + \left(\frac{1}{K_{LH}} - C_b + \frac{\delta_L \rho_{cat} \bar{k}}{\beta_m}\right) C_s - \frac{C_b}{K_{LH}} = 0 \tag{11}$$

Eqn (11) has two analytical solutions, which read:

$$C_{s1/2} = -\frac{1}{2}\left(\frac{1}{K_{LH}} - C_b + \frac{\delta_L \rho_{cat} \bar{k}}{\beta_m}\right) \pm \sqrt{\frac{1}{4}\left[\frac{1}{K_{LH}} - C_b + \frac{\delta_L \rho_{cat} \bar{k}}{\beta_m}\right]^2 + \frac{C_b}{K_{LH}}} \tag{12}$$

Apparently, one of the two solutions of eqn (12) is negative, and hence only the positive one is meaningful, which reads:

$$C_s = -\frac{1}{2}\left(\frac{1}{K_{LH}} - C_b + \frac{\delta_L \rho_{cat} \bar{k}}{\beta_m}\right) + \sqrt{\frac{1}{4}\left[\frac{1}{K_{LH}} - C_b + \frac{\delta_L \rho_{cat} \bar{k}}{\beta_m}\right]^2 + \frac{C_b}{K_{LH}}} \tag{13}$$

Relating R_{obs} to the surface concentration C_s transforms eqn (9) into the form:

$$\frac{dC_b}{dz} = -\frac{1}{\dot{V} L_{MR}} \frac{\bar{k} m_{cat} K_{LH} C_s}{1 + K_{LH} C_s} \tag{14}$$

Substituting C_s from eqn (13) into this equation eliminates the unknown surface concentration by relating it to the bulk concentration and the mass transfer coefficient β_m. The mass transfer coefficient β_m can be calculated from an established empirical correlation for laminar flow in microchannels using the Sherwood number Sh, Reynolds number Re and Schmidt number Sc (details in ESI† S15):[53]

$$Sh = \frac{\beta_m d_h}{D_{RhB}} = 7.54\left(1 + 0.095 \frac{d_h}{L_{MR}} ReSc\right)^{0.45} \tag{15}$$

$$Re = \frac{\bar{u} d_h}{\nu} \tag{16}$$

$$Sc = \frac{\nu}{D_{RhB}} \tag{17}$$

where d_h [m] is the hydraulic diameter of the channel, D_{RhB} [m^2 s^{-1}] is the binary diffusion coefficient of the pollutant RhB in water, ν [m^2 s^{-1}] is the kinematic viscosity of water and $\bar{u}$ [m s^{-1}] is the mean flow velocity in the channel. This finally allows to solve eqn (14) with the Matlab® routine ODE45 to obtain the concentration profile of the pollutant along the microchannel.

4. Results and discussion

4.1. Immobilization of the TiO_2 films

Droplet generation during inkjet-printing was investigated by adjusting the piezoelectric actuating parameters of the nozzle including the pulse voltage and length. These two parameters can be tuned to adjust the size and jetting velocity of the droplets.[41] Fig. 4 shows exemplarily the influence of the pulse voltage and length on the droplet size for the developed ink. Typically, the higher the applied actuation energy the higher is the amount of the entrained ink from the nozzle, resulting in an increase of the drop diameter with increasing voltage. Based on the aforementioned arguments, in this study, a pulse voltage of 41 V and length of 40 μs was used for printing the TiO_2 ink, and the droplet size was 83 μm (determined using the CCD camera). By knowing the droplet size, the loaded mass of the TiO_2 printed on a certain area can be calculated:

$$m_{cat} = N_l \cdot \frac{l_x}{i_x} \cdot \frac{l_y}{i_y} \cdot \frac{4}{3}\pi \left(\frac{d}{2}\right)^3 \cdot \rho_{ink} \cdot C_{ink} \tag{18}$$

This journal is © The Royal Society of Chemistry 2020

Open Access Article. Published on 11 August 2020. Downloaded on 4/29/2026 1:24:24 PM.
This article is licensed under a Creative Commons Attribution-NonCommercial 3.0 Unported Licence.

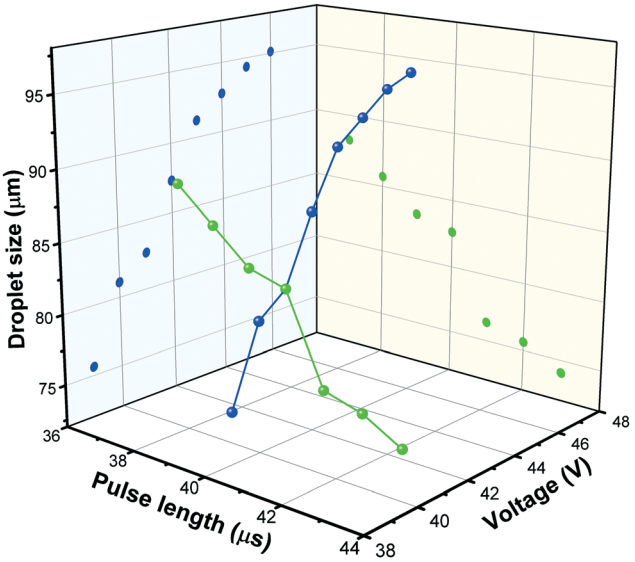

Fig. 4 Droplet size change with variation of pulse length and voltage.

where N_l is the total number of printed layers, l_x and l_y is the length of the printing area in x- and y-direction, i_x and i_y is the distance between two droplets in x- and y-direction as set in the printer, d is the droplet diameter, ρ_{ink} is ink density (1.07 g mL^{-1}) and C_{ink} represents the catalyst concentration of the ink suspension (0.5 wt%). For the 2.5 cm × 2.5 cm substrate, by setting the droplet distance to 105 µm, according to eqn (18), the catalyst loading per layer is m_{cat} = 0.09 mg. Directly comparing the calculated catalyst mass with the weighted mass of the printed layer was not possible, since the value of the mass per layer is considerably low. However, the change of the droplet size was observed to be negligible before and after printing, which ensures a precise control of the loaded mass per layer. Moreover, a previous study in our group also proved a precise control of the loaded mass with the same device for inkjet-printing of Al_2O_3.[41]

4.2. Characterization of the TiO_2 films

Fig. 5(a) shows that the printed TiO_2 layer is highly porous, and the particles do not aggregate to form bigger sintered particles but only agglomerate slightly, which was also reported elsewhere.[46] Fig. 5(b) shows that the printed layer exhibits a thickness between 0.72 µm and 1.42 µm in the extracted area in the SEM image, which also matches the measured range of thickness (see also below and ESI† S7). The observed asymmetric structure of the ceramic substrate is in accordance with the aforementioned information provided by the substrate manufacturer.

Since the printed TiO_2 layer is not uniform in thickness within the small extracted area analyzed *via* electron probe microanalysis (Fig. 5(b)), optical profilometry was employed to determine the average thickness of a larger selected area

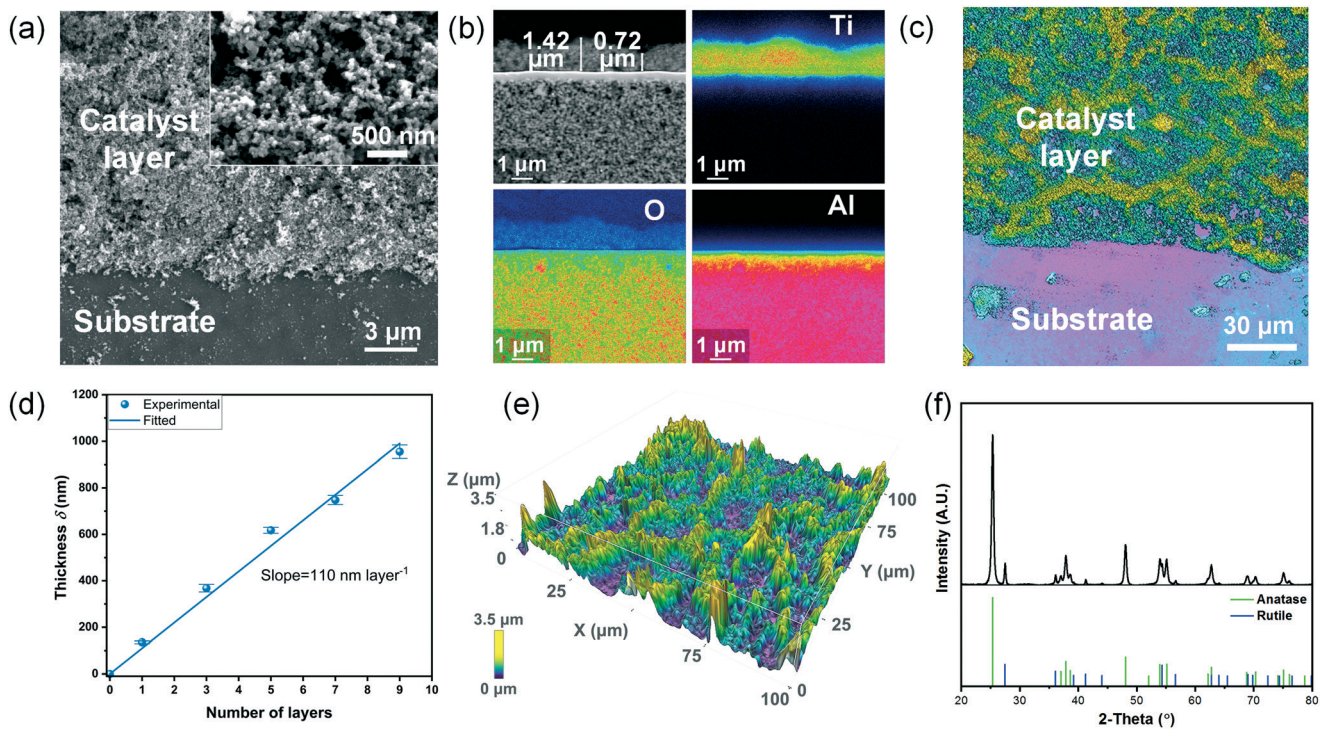

Fig. 5 Characterization results of the printed coating after calcination at 250 °C: (a) top-view SEM image of the catalyst layer on the ceramic substrate; (b) element distribution map of the ceramic substrate coated with 9 layers of TiO_2 in cross-section (from blue to red: increasing signal intensity); (c) 2-D surface morphology of a 9-layer coating; (d) layer thickness as a function of the number of layers (data given are mean values of $n \geq 3$ replicates, error bar: standard error of the mean); (e) 3D morphology of the coating; (f) XRD result of the TiO_2 powder obtained after calcining the ink at 250 °C.

Open Access Article. Published on 11 August 2020. Downloaded on 4/29/2026 1:24:24 PM.
This article is licensed under a Creative Commons Attribution-NonCommercial 3.0 Unported Licence.

of *ca.* 0.1–0.3 mm^2. In order to obtain a higher contrast and hence to reliably determine the layer thickness using the confocal mode, glass was used as the substrate for this analysis. Fig. 5(c) illustrates the contrast between the printed catalyst layer and the glass substrate. As Fig. 5(d) illustrates, a clear linearity is found between the mean layer thickness and the number of layers, which indicates that good control over the mean layer thickness is achieved by the inkjet-printing. The slope reveals that the thickness per layer is around 110 nm. However, the surface is rather rough (RMS roughness = 0.6 μm, Fig. 5(e)) and locally shows some non-uniformity as mentioned above.

The porosity of the layer was calculated to be 0.69 by:

$$\varepsilon = 1 - \frac{m_L}{\rho_L \delta_L A_{cat}} \quad (19)$$

where m_L is the catalyst mass at layer thickness δ_L which was calculated from eqn (18), ρ_L is the bulk density of TiO_2 P25, which is 4.26 g cm^{-3} (from manufacturer), and A_{cat} is the area of the coating. The calculated value is in perfect accordance with the one reported in literature for a thin film of TiO_2 P25 prepared by doctor blading.[54] The density of the coated thin film can be calculated with eqn (20) by knowing m_L, δ_L and A_{cat}, which yields 1.31 g cm^{-3}.

$$\rho_{cat} = \frac{m_L}{\delta_L A_{cat}} \quad (20)$$

As shown in Fig. 5(f), the powder XRD pattern reveals that the composition of the ink after calcination at 250 °C is still anatase and rutile. By employing the reference intensity ratio (RIR) method,[55] the phase composition of anatase and rutile was calculated to be 83% and 17%, respectively. This result is in accordance with the previously reported composition for pristine TiO_2 P25, and is in the same range as generally known (80 : 20 in anatase and rutile) for this product.[56,57] This proves that calcination did not cause a change in phases. In addition, XPS analysis has shown that sodium was present in the coating which could be a result of additives present in the ink (ESI† Fig. S13). The presence of sodium may influence catalyst activity *via* doping effects. To clarify this point further studies would be needed.

4.3. Assessment of the reaction kinetics

4.3.1. Analysis of possible mass transport limitations. As already stated in section 3.2, the results of the batch reactor experiments were checked for the influence of external mass transport by variation of the stirring speed. As shown in Fig. 6, increasing the stirring speed from 200 to 400 rpm didn't yield a significant difference in the degradation over time, indicating that film diffusion limitation can already be excluded for the standard stirring speed of 200 rpm used in this work.

To investigate the possible influence of pore diffusion limitation, the Weisz–Prater criterion given in eqn (8) in section 3.2 was employed. For evaluating eqn (8), the effective diffusivity D_{eff} was estimated according to the well-known formula:

$$D_{eff} = \frac{\varepsilon D_{RhB}}{\tau} \quad (21)$$

where D_{RhB} is the binary diffusion coefficient of the pollutant RhB in water, ε is the porosity and τ is the tortuosity factor. ε = 0.69 was taken from the characterization of the printed layer while τ = 3 and D_{RhB} = 4.27 × 10^{-10} m^2 s^{-1} were retrieved from literature.[58,59] The Weisz modulus for different layer thickness at the end of the respective experiments (where the concentration and the limiting value are supposed to be the lowest) can be calculated according to eqn (8), as shown in Table 2. Note that the limiting values were determined for different values of $K_{LH}C$ based on the study by Satterfield,[51,52] and for K_{LH} a value of 0.14 m^3 g^{-1} which was obtained by fitting as presented in 4.3.2. Besides, the observed reaction rate necessary for calculating ψ_{WP} was obtained from the fitted curves for the observed degradation as presented in Fig. 8.

It is can be seen that all the values of ψ_{WP} are lower than their corresponding limiting values. This indicates that internal mass transport limitations can be neglected.

4.3.2. Determination of the kinetic parameters. First, to determine the extinction coefficient ω (eqn (3)), the measured transmission T_L for different layer thickness was used, as shown in Fig. 7. By employing a linear least squares fitting, a value of ω = 4.38 × 10^6 m^{-1} was obtained.

Fig. 8 illustrates the experimental data of the degradation by a coating of 9 layers (δ_L = 990 nm) at initial concentrations varying from 3 to 15 g m^{-3} and by coatings of various layer thicknesses with an initial concentration of 15 g m^{-3}. Based on the 9 groups of experimental data, a non-linear fitting according to eqn (7) has been conducted for determining the

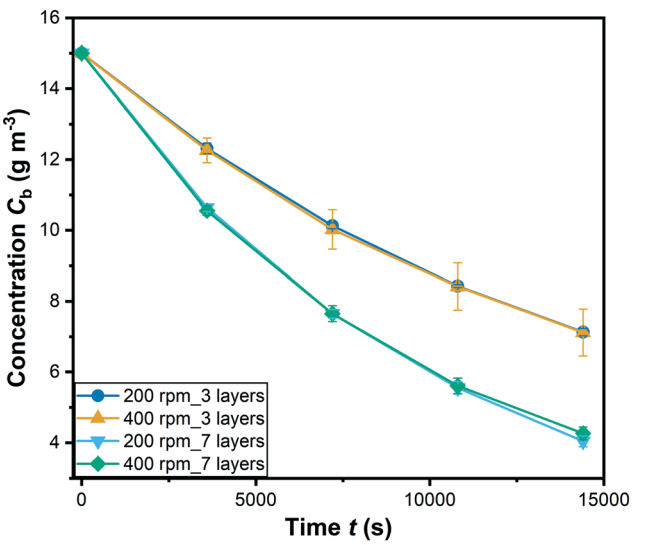

Fig. 6 Degradation of RhB with different coating at 200 and 400 rpm stirring speed (C_0 = 15 g m^{-3}; symbols: mean values of 3 replicates; error bars: standard error of the mean).

This journal is © The Royal Society of Chemistry 2020

Open Access Article. Published on 11 August 2020. Downloaded on 4/29/2026 1:24:24 PM.
This article is licensed under a Creative Commons Attribution-NonCommercial 3.0 Unported Licence.

Table 2 Calculated Weisz modulus and limiting values for different layer thickness at the end of each experiment

Thickness (m)	Limiting value	ψ_{WP}
1.1×10^{-7}	0.40	0.002
3.3×10^{-7}	0.34	0.021
5.5×10^{-7}	0.31	0.056
7.7×10^{-7}	0.28	0.103
9.9×10^{-7}	0.25	0.153

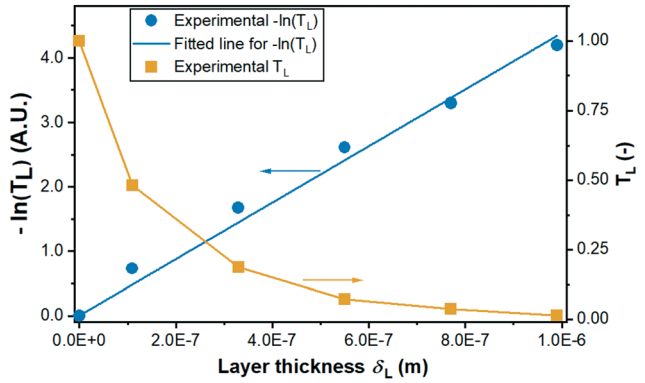

Fig. 7 Experimental data and fitting of measured transmission T_L and $-\ln(T_L)$ *versus* layer thickness for determining the extinction coefficient ω.

kinetic parameters which are summarized in Table 3. Note that the estimation of the 3 kinetic parameters a, b, and K_{LH} was conducted for all experimental data shown in Fig. 8 together in one run (see section 3.2). The data include different layer thicknesses and initial concentrations. Apparently, the kinetic model predicts a bit low reaction rates for high layer thickness and high initial concentration, but overall the fit is considered satisfactory, also with a view to the confidence intervals and correlation coefficients for the parameter estimates. The fitted curves are shown in Fig. 8 and the kinetic parameters with the individual linearized confidence intervals at a confidence level of $P = 0.95$ are summarized in Table 4. Besides, as shown in the correlation matrix as well as the plots of the pairwise joint linearized confidence regions illustrating the correlation between each two parameters (ESI† Fig. S14), a and b, as well as K_{LH} and b present only a moderate correlation. On the contrary, K_{LH} correlates significantly to a. This negative correlation can be explained by combing eqn (4) and (5): keeping the reaction rate constant, higher a yields a lower K_{LH}. As shown in section 4.4, the model is able to reproduce not only the influence of the layer thickness but also of the incident light intensity on the reaction rate correctly.

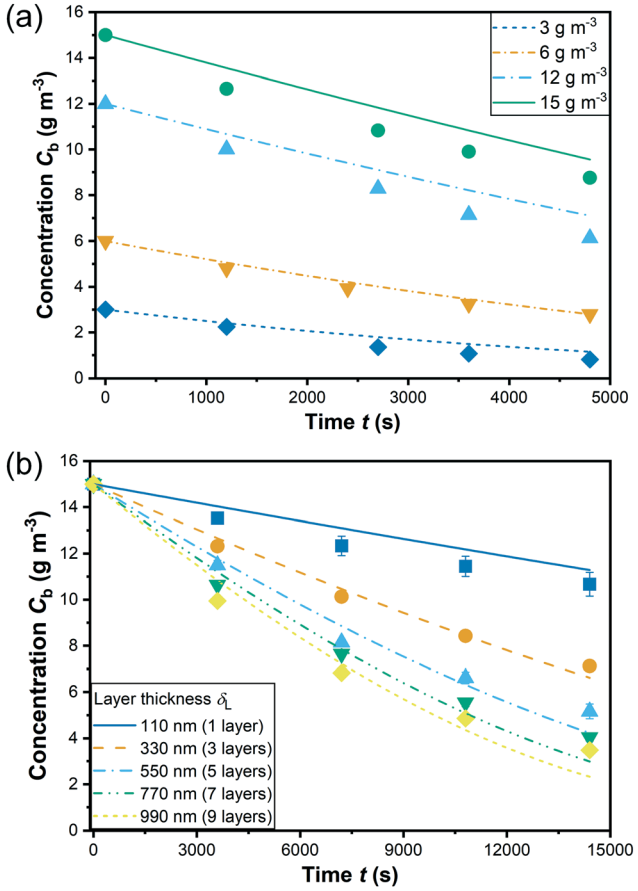

Fig. 8 Degradation with (a) 9-layer coating (990 nm thickness) at different initial concentrations; (b) coatings of different thickness (symbols: mean values of measured data of $n \geq 3$ replicates; error bars: standard error of the mean; lines: fitting).

The adsorption equilibrium constant K_{LH} was determined to be 0.14 $m^3\ g^{-1}$. A large number of studies from literature describe the photocatalytic degradation with a pseudo first-order kinetic model assuming that $K_{LH}C \ll 1$.[30,42,49] However, for the present study, the term $K_{LH}C$ is close to or even larger than 1, which obviously cannot be neglected.

4.4. Kinetic performance in the microreactor

The derived kinetic model was used to analyze the results of the continuous-flow microreactor experiments. For this purpose, the conversion X of the pollutant [%] was evaluated:

$$X = \frac{C_0 - C}{C_0} \tag{22}$$

Table 3 Kinetic parameters determined from a non-linear fitting to the experimental data

	Value	Confidence interval at confidence level of 0.95
a [g $cm^{0.86}$ g^{-1} s^{-1} $mW^{-0.43}$]	4.01×10^{-5}	7.09×10^{-7}
b [−]	0.43	0.013
K_{LH} [m^3 g^{-1}]	0.14	0.005

Open Access Article. Published on 11 August 2020. Downloaded on 4/29/2026 1:24:24 PM.
This article is licensed under a Creative Commons Attribution-NonCommercial 3.0 Unported Licence.

Table 4 Correlation matrix of the determined kinetic parameters (unit not shown)

	a	b	K_{LH}
$\boldsymbol{a}$	1.00	−0.48	−0.98
$\boldsymbol{b}$	0	1.00	0.51
$\boldsymbol{K_{LH}}$	0	0	1.00

Here, C_0 is the inlet concentration and C is the measured outlet concentration. An exemplary illustration of the development of the outlet concentration with experiment time for three data series with different operational parameters is displayed in Fig. 9. Keeping the flow rate and light intensity constant, lower initial concentration led to a higher conversion (X), as shown in the upper part of Fig. 9. The lower part of Fig. 9 indicates that the reactor performance was stable for at least 3 hours after the concentration became constant. Note that the equilibrating time for the low flow rate of 0.05 mL min^{-1} is much longer than the one for 0.2 mL min^{-1}. Table 5 summarizes the degradation results with variation of the operational parameters.

As explained in section 3.2, internal diffusion limation could be ruled out also for the microreactor experiments based on the assessment of the Weisz modulus. On the contrary, external mass transport was explicitely considered according to eqn (13)–(17), which allowed to simulate the degradation in the microreactor. The simulated bulk concentration C_b and concentration on the external surface of the catalyst layer C_s for one experiment are illustrated in Fig. 10(a), showing the influence of the external mass transport. The predicted conversion for all experiments is compared to the experimental results listed in Table 5, as shown in a parity plot given in Fig. 10(b). All data points fall

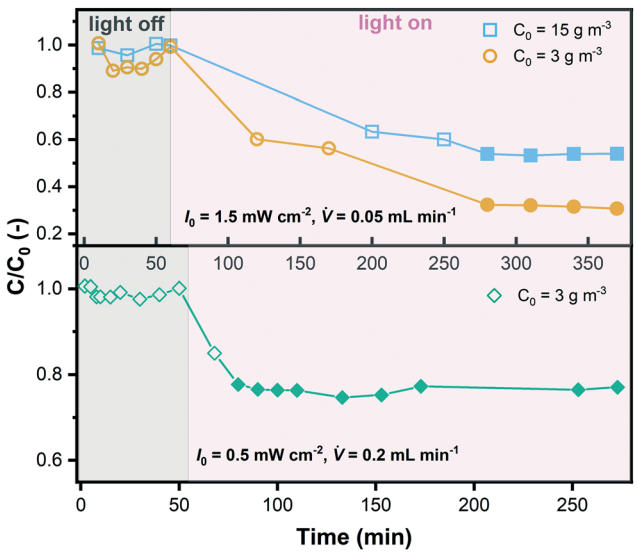

Fig. 9 An exemplary display of the outlet concentration with experiment time in the microreactor for 3 different data series (filled symbols represent the points used for data evaluation).

Table 5 Degradation X [%] in the microreactor by varying the light intensity I_0 [mW cm^{-2}], inlet concentration C_0 [g m^{-3}] and flow rate $\dot{V}$ [mL min^{-1}]

	C_0 = 15		C_0 = 3	
	I_0 = 0.5	I_0 = 1.5	I_0 = 0.5	I_0 = 1.5
$\dot{V}$ = **0.05**	34	47	60	71
$\dot{V}$ = **0.1**	21	32	40	53
$\dot{V}$ = **0.2**	12	20	23	35

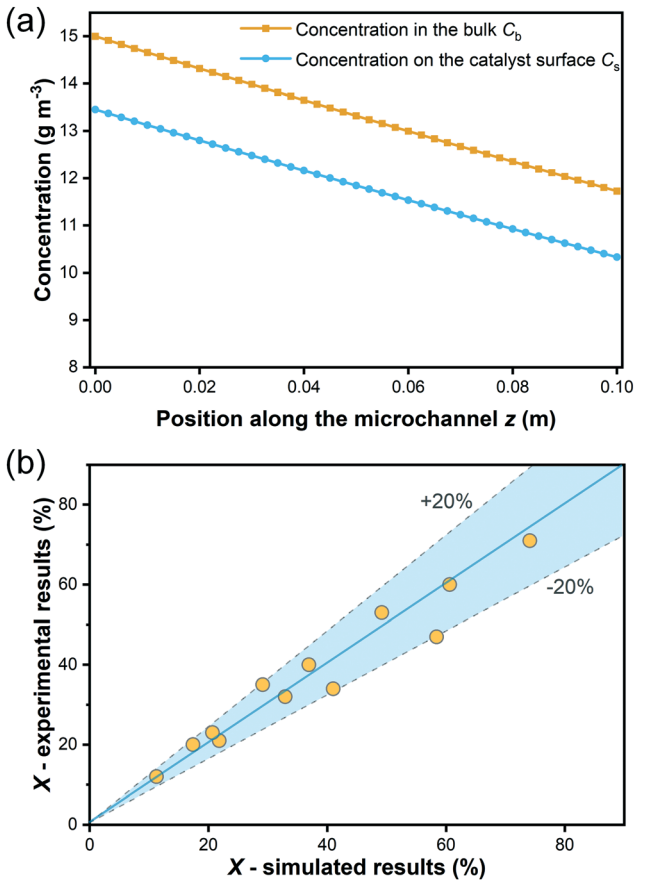

Fig. 10 (a) Illustration of the bulk concentration C_b and concentration on the external surface of the catalyst layer C_s along the microchannel (experimental condition: C_0 = 15 g m^{-3}, I_0 = 0.5 mW cm^{-2}, $\dot{V}$ = 0.1 mL min^{-1}); (b) comparison of the simulative and experimental results in a parity plot for the microreactor experiment.

inside the ±20% region, indicating that the simulated results match the experimental results well, and hence the determined kinetic model is validated.

5. Conclusions

In this work, a kinetic study of the degradation of the model pollutant rhodamine B (RhB) on inkjet-printed TiO_2 coatings was conducted. Inkjet-printing was found quite suitable for precisely controlling the thickness and loaded mass of the coated layer with 110 nm and 0.09 mg per layer, respectively, which is a prerequisite for a valid kinetic study. A Langmuir–

This journal is © The Royal Society of Chemistry 2020

Open Access Article. Published on 11 August 2020. Downloaded on 4/29/2026 1:24:24 PM.
This article is licensed under a Creative Commons Attribution-NonCommercial 3.0 Unported Licence.

Hinshelwood type kinetic model considering the influence of the light attenuation inside the catalyst layer proved suitable to describe the experimental data. First, parameters estimated for the kinetic constants could be established from batch reactor data. External and internal mass transport limitations could be ruled out for the underlying data. The obtained estimates therefore characterize the intrinsic chemical kinetics. Unlike most published studies for photocatalytic degradation using a pseudo first-order kinetic model under the assumption of $K_{LH}C \ll 1$, the adsorption equilibrium constant K_{LH} determined here is large resulting in $K_{LH}C$ being close to 1 or even larger, meaning that the reaction cannot be simplified to a first-order reaction.

The kinetic model was further validated using a novel microreactor system with fiber optics for precise light introduction in continuous-flow mode under variation of the light intensity, flow rate and inlet concentration. Simulated results match the experimentally determined values well without any adjustments of the parameters, which confirms that the reaction kinetics is independent of the reactor system if the kinetic analysis is properly done.

The present work provides an approach for kinetic studies on photocatalytic degradation. It is worth noting though that RhB in water used in this work is a model pollutant. For other pollutants or mixtures of pollutants and for more complex media the description of mass transport and also of the reaction kinetics may be significantly more challenging which adds complexity both to the kinetic model and to the reactor modelling. However, if all important effects are properly considered in the modelling and if the experimental system enables kinetic studies under well-defined conditions, the derived reaction kinetics should still be transferable to other reactor systems, *e.g.*, for scale-up purposes. In that spirit, further work utilizing the novel microreactor system presented in this study includes investigations on the degradation of additional types of pollutants relevant for water treatment, in particular pharmaceutical micropollutants, coupling of photocatalytic degradation with membrane filtration, and testing of novel photocatalysts with high activity in the range of visible light. Besides, this system will be used for studies of other topics such as photocatalytic organic synthesis.

Conflicts of interest

There are no conflicts to declare.

Acknowledgements

The authors would like to acknowledge the funding from the strategic NanoMembrane initiative within the Helmholtz Program – Science and Technology of Nanosystems (STN). Fruitful discussions with Prof. Bryce Richards, Tobias Berger, Roman Lyubimenko and other colleagues from the NanoMembrane initiative are acknowledged. X. Z. is grateful to Ms. Gabriele Straass (Mountain Photonics) for the help in the light source setup and Mr. Paul Kant for the help in MATLAB simulation. Frank Kirschhöfer and Gerald Brenner-Weiß (IFG, KIT) are acknowledged for their helpful suggestions.

References

1 C. J. L. Murray and A. D. Lopez, *Lancet*, 1997, **349**, 1436–1442.
2 E. Diamanti-Kandarakis, J.-P. Bourguignon, L. C. Giudice, R. Hauser, G. S. Prins, A. M. Soto, R. T. Zoeller and A. C. Gore, *Endocr. Rev.*, 2009, **30**, 293–342.
3 A. C. Johnson and J. P. Sumpter, *Environ. Sci. Technol.*, 2001, **35**, 4697–4703.
4 D. Cambie, C. Bottecchia, N. J. Straathof, V. Hessel and T. Noel, *Chem. Rev.*, 2016, **116**, 10276–10341.
5 M. Gmurek, M. Olak-Kucharczyk and S. Ledakowicz, *Chem. Eng. J.*, 2017, **310**, 437–456.
6 M. N. Chong, B. Jin, C. W. K. Chow and C. Saint, *Water Res.*, 2010, **44**, 2997–3027.
7 A. J. C. Semião and A. I. Schäfer, *J. Membr. Sci.*, 2013, **431**, 244–256.
8 L. D. Nghiem, A. Manis, K. Soldenhoff and A. I. Schäfer, *J. Membr. Sci.*, 2004, **242**, 37–45.
9 A. Imbrogno and A. I. Schäfer, *J. Membr. Sci.*, 2019, **585**, 67–80.
10 M. Tagliavini and A. I. Schäfer, *J. Hazard. Mater.*, 2018, **353**, 514–521.
11 X. Li, F. I. Hai and L. D. Nghiem, *Bioresour. Technol.*, 2011, **102**, 5319–5324.
12 S. Esplugas, J. Giménez, S. Contreras, E. Pascual and M. Rodríguez, *Water Res.*, 2002, **36**, 1034–1042.
13 X. Chen and S. S. Mao, *Chem. Rev.*, 2007, **107**, 2891–2959.
14 S. Mozia, *Sep. Purif. Technol.*, 2010, **73**, 71–91.
15 S. Carbonaro, M. N. Sugihara and T. J. Strathmann, *Appl. Catal., B*, 2013, **129**, 1–12.
16 I. Fasaki, K. Siamos, M. Arin, P. Lommens, I. Van Driessche, S. C. Hopkins, B. A. Glowacki and I. Arabatzis, *Appl. Catal., A*, 2012, **411-412**, 60–69.
17 Z. Meng, X. Zhang and J. Qin, *Nanoscale*, 2013, **5**, 4687–4690.
18 C. Regmi, S. Lotfi, J. C. Espíndola, K. Fischer, A. Schulze and A. I. Schäfer, *Catalysts*, 2020, **10**, 725.
19 H. C. Aran, D. Salamon, T. Rijnaarts, G. Mul, M. Wessling and R. G. H. Lammertink, *J. Photochem. Photobiol., A*, 2011, **225**, 36–41.
20 I. Horovitz, D. Avisar, M. A. Baker, R. Grilli, L. Lozzi, D. Di Camillo and H. Mamane, *J. Hazard. Mater.*, 2016, **310**, 98–107.
21 G. E. Romanos, C. P. Athanasekou, F. K. Katsaros, N. K. Kanellopoulos, D. D. Dionysiou, V. Likodimos and P. Falaras, *J. Hazard. Mater.*, 2012, **211-212**, 304–316.
22 S. Sanches, C. Nunes, P. C. Passarinho, F. C. Ferreira, V. J. Pereira and J. G. Crespo, *J. Chem. Technol. Biotechnol.*, 2017, **92**, 1727–1737.
23 T. E. Berger, C. Regmi, A. I. Schäfer and B. S. Richards, *J. Membr. Sci.*, 2020, **604**, 118015.

Open Access Article. Published on 11 August 2020. Downloaded on 4/29/2026 1:24:24 PM.
This article is licensed under a Creative Commons Attribution-NonCommercial 3.0 Unported Licence.

24 A. Visan, D. Rafieian, W. Ogieglo and R. G. H. Lammertink, *Appl. Catal., B*, 2014, **150-151**, 93–100.
25 D. Chen, F. Li and A. K. Ray, *AIChE J.*, 2000, **46**, 1034–1045.
26 E. E. Coyle and M. Oelgemoller, *Photochem. Photobiol. Sci.*, 2008, **7**, 1313–1322.
27 T. Van Gerven, G. Mul, J. Moulijn and A. Stankiewicz, *Chem. Eng. Process.*, 2007, **46**, 781–789.
28 M. Krivec, K. Žagar, L. Suhadolnik, M. Čeh and G. Dražić, *ACS Appl. Mater. Interfaces*, 2013, **5**, 9088–9094.
29 S. Das and V. C. Srivastava, *Photochem. Photobiol. Sci.*, 2016, **15**, 714–730.
30 H. Maleki and V. Bertola, *ACS Appl. Nano Mater.*, 2019, **2**, 7237–7244.
31 T. Claes, A. Dilissen, M. E. Leblebici and T. Van Gerven, *Chem. Eng. J.*, 2019, **361**, 725–735.
32 A. Visan, J. R. van Ommen, M. T. Kreutzer and R. G. H. Lammertink, *Ind. Eng. Chem. Res.*, 2019, **58**, 5349–5357.
33 A. K. Ray and A. A. C. M. Beenackers, *AIChE J.*, 1997, **43**, 2571–2578.
34 D. Chen and A. K. Ray, *Appl. Catal., B*, 1999, **23**, 143–157.
35 S. Zhou and A. K. Ray, *Ind. Eng. Chem. Res.*, 2003, **42**, 6020–6033.
36 D. Chen, F. Li and A. K. Ray, *Catal. Today*, 2001, **66**, 475–485.
37 M. Melchionna and P. Fornasiero, *ACS Catal.*, 2020, **10**, 5493–5501.
38 M. Qureshi and K. Takanabe, *Chem. Mater.*, 2016, **29**, 158–167.
39 M. Singh, H. M. Haverinen, P. Dhagat and G. E. Jabbour, *Adv. Mater.*, 2010, **22**, 673–685.
40 A. K. Mogalicherla, S. Lee, P. Pfeifer and R. Dittmeyer, *Microfluid. Nanofluid.*, 2014, **16**, 655–666.
41 M. Siebert, R. R. Zimmermann, M. Armbrüster and R. Dittmeyer, *ChemCatChem*, 2017, **9**, 3733–3742.
42 M. L. Satuf, J. Macagno, A. Manassero, G. Bernal, P. A. Kler and C. L. A. Berli, *Appl. Catal., B*, 2019, **241**, 8–17.
43 D. Rafieian, R. T. Driessen, W. Ogieglo and R. G. Lammertink, *ACS Appl. Mater. Interfaces*, 2015, **7**, 8727–8732.
44 G. Charles, T. Roques-Carmes, N. Becheikh, L. Falk, J.-M. Commenge and S. Corbel, *J. Photochem. Photobiol., A*, 2011, **223**, 202–211.
45 T. H. Rehm, S. Gros, P. Löb and A. Renken, *React. Chem. Eng.*, 2016, **1**, 636–648.
46 R. Cherrington, D. J. Hughes, S. Senthilarasu and V. Goodship, *Energy Technol.*, 2015, **3**, 866–870.
47 D. D. Phan, F. Babick, M. T. Nguyen, B. Wessely and M. Stintz, *Chem. Eng. Sci.*, 2017, **173**, 242–252.
48 K. V. Kumar, K. Porkodi and F. Rocha, *Catal. Commun.*, 2008, **9**, 82–84.
49 J.-M. Herrmann, *Catal. Today*, 1999, **53**, 115–129.
50 A. Jess, P. Wasserscheid and W. John and Sons, *Chemical technology : an integral textbook*, Wiley-Vch, Weinheim, 2013.
51 G. Ertl, H. Knözinger, F. Schüth and J. Weitkamp, *Handbook of Heterogeneous Catalysis*, Chapter 6.3, vol. 8, Wiley, 2008.
52 C. N. Satterfield, *Mass Transfer in Heterogeneous Catalysis*, Chapters 3 & 4, M.I.T. Press, Cambridge, MA, 1970.
53 N. Kockmann, *Transport Phenomena in Micro Process Engineering*, Chapter 6.2, Springer, Berlin Heidelberg, 2007.
54 H. Lindström, E. Magnusson, A. Holmberg, S. Södergren, S.-E. Lindquist and A. Hagfeldt, *Sol. Energy Mater. Sol. Cells*, 2002, **73**, 91–101.
55 C. R. Hubbard and R. L. Snyder, *Powder Diffr.*, 2013, **3**, 74–77.
56 D. M. Tobaldi, R. C. Pullar, M. P. Seabra and J. A. Labrincha, *Mater. Lett.*, 2014, **122**, 345–347.
57 B. Ohtani, O. O. Prieto-Mahaney, D. Li and R. Abe, *J. Photochem. Photobiol., A*, 2010, **216**, 179–182.
58 N. Padoin and C. Soares, *Chem. Eng. J.*, 2017, **310**, 381–388.
59 C. T. Culbertson, S. C. Jacobson and J. Michael Ramsey, *Talanta*, 2002, **56**, 365–373.

This journal is © The Royal Society of Chemistry 2020